

# Real-time control of the deposition location of ECRH in the LHD

T. Ii Tsujimura<sup>a,\*</sup>, Y. Mizuno<sup>a</sup>, R. Yanai<sup>a</sup>, T. Tokuzawa<sup>a,b</sup>, Y. Ito<sup>a</sup>, M. Nishiura<sup>a</sup>, S. Kubo<sup>a</sup>, T. Shimozuma<sup>a</sup>, Y. Yoshimura<sup>a</sup>, H. Igami<sup>a</sup>, H. Takahashi<sup>a,b</sup>, K. Tanaka<sup>a</sup>, M. Yoshinuma<sup>a</sup>, S. Ohshima<sup>c</sup>, the LHD Experiment Group<sup>a</sup>

<sup>a</sup>National Institute for Fusion Science, National Institutes of Natural Sciences, Toki, Gifu 509-5292, Japan

<sup>b</sup>The Graduate University for Advanced Studies, SOKENDAI, Toki, Gifu 509-5292, Japan

<sup>c</sup>Institute of Advanced Energy, Kyoto University, Uji, Kyoto 611-0011, Japan

---

## Abstract

A real-time control system for the deposition location of electron cyclotron resonance heating (ECRH) has been newly developed and applied to experiments on the Large Helical Device (LHD). Appropriate settings for a steerable launcher for ECRH were obtained by evaluating the deposition location and the absorption power for various electron density profiles using a ray-tracing code. The real-time deposition location control system adjusts launcher settings to improve the first-pass absorption of the refracted electron cyclotron wave, based on the ray-tracing calculations. The control system was designed to use a fast field programmable gate array (FPGA). The FPGA processes in real time the calculation of characteristic parameters regarding the density profile and the calculation of target positions requested for rotation control of a steering mirror of the launcher. The real-time deposition location control during ECRH discharges on the LHD functioned successfully in maintaining the absorption power higher than that without the control, which resulted from the deposition location maintained in the plasma core region.

**Keywords:** ECRH, deposition location, real-time control, ray tracing, FPGA, LHD

---

## 1. Introduction

Adjustments of launcher settings of electron cyclotron resonance heating and current drive (ECRH/ECCD) are necessary to produce high-performance plasmas, to realize desired power deposition and current density profiles, to decrease the stray wave radiation level in the vessel, and to prevent damage of in-vessel components from unabsorbed power during high-power long-pulse injection [1]. Real-time deposition location control of ECCD is demonstrated to be effective for active MHD control of tokamaks [2, 3, 4]. Prediction of deposition profiles by ray-tracing calculations can help adjustments of ECRH launcher settings to maximize the first-pass power absorption. The precise evaluation of deposition profiles is also essential for transport studies. Power-modulated ECRH is used to generate heat pulses in order to evaluate cross-field electron thermal transport [5]. Several attempts are made to adjust the deposition location and the incident ECRH polarization in the Large Helical Device (LHD) [1, 6], which contributes to extending the operation regime of high electron-temperature ( $T_e$ ) plasmas and also to analyzing electron heat transport properties of hydrogen isotope plasmas [7, 8, 9].

In such types of experiments, ray-tracing calculations with the “LHDGauss” code have been utilized on a shot-by-shot basis [10] because the code is implemented on the automatic analysis system for post-shot processing on the LHD [11]. The LHDGauss code can provide not only the deposition profiles

for the ordinary (O) mode and the extraordinary (X) mode but also the ratio between the two orthogonal eigenmodes at the electron cyclotron resonance (ECR) layer. The ratio between the two modes is calculated by solving the one-dimensional (1D) full-wave equation along the wave propagation to the ECR layer from each launching antenna at which the incident polarization is given.

With the help of the LHDGauss code, real-time control of the incident polarization was conducted for the time-varying electron-density ( $n_e$ ) profile of LHD plasmas [12]. The control method is based on the mode content analysis to excite the pure O mode or the pure X mode at the ECR layer. The data set on the dependence of the optimum polarization on peripheral  $n_e$  profiles as well as the relationship between the optimum polarization and the set of rotation angles of the two polarizers in the ECRH transmission line were saved into FPGA (field programmable gate array) memories. The stored data in these FPGA memories were referred to in real time for rotation control of the polarizers. The polarizer control experiments functioned properly in exciting the purer heating mode, so that the first-pass absorption power could be maintained higher than that without the control. However, a gradual increase of  $n_e$  in time gave rise to the electron cyclotron (EC) wave refracted to the outside of the ECR layer, thereby decreasing the first-pass absorption power, although the pure mode was excited due to the control under the LHDGauss calculation. **It is noted that the O/X-mode ratio was calculated only along the straight line in 1D from the center of the final mirror of the launcher to the target position. When  $n_e$  is high enough to refract the EC wave, the EC wave propagates on the path deviating from the straight**

---

\*Corresponding author

Email address: tsujimura.tohru@nifs.ac.jp (T. Ii Tsujimura)

line. The incident polarization could be optimized only on the straight line, not on the refracted beam path. The experimental results show that the effect of multi-pass absorption power cannot be neglected. However, optimizing the polarization for the second-pass absorption is difficult under the present situation. Thus, deposition location control is required to improve the first-pass absorption under the effect of refraction taken into account. This paper describes real-time control of the deposition location of ECRH using the newly-developed real-time control system. Section 2 describes the detail of the real-time control system of the deposition location. Results on proof-of-principle experiments of the real-time deposition location control are presented and discussed in Section 3. Section 4 summarizes this paper. It is noted that the polarization control was not implemented in the present study.

## 2. Real-time control system of the deposition location of ECRH

The LHD is a helical device with the toroidal period of 10 and the poloidal period of 2. The confinement magnetic field is generated by external superconducting magnets with a pair of helical coils and three pairs of poloidal coils. The fundamental O mode at 77 GHz and the second harmonic X mode at 154 GHz are used for plasma electron heating under the standard magnetic field configuration of the magnetic axis of 3.6 m. The magnetic field strength at the axis was set 2.75 T, which is the cold resonant field strength of ECRH [13]. Since the fundamental X-mode EC wave at 77 GHz is reflected at the right-hand cutoff layer in front of the ECR layer in this experiment condition, excitation of the pure O mode contributes to higher first-pass absorption of the EC wave. The launching antenna used for real-time control of the deposition location is located at the lower (L) right (R) side of an equatorial outer port (2-O), and the antenna is called the 2-OLR antenna. The 2-OLR antenna was designed for power injection from a 77-GHz gyrotron. Figure 1(a) shows a drawing viewed from the center of the final mirror of the 2-OLR antenna. Most parts of the first wall consist of protecting tiles made of stainless steel, but some tiles are replaced by molybdenum on the opposite side of the launching antennas. In the drawing, an imaginary grid target plane is shown with a toroidally- and vertically-directed coordinate  $(T_f, Z_f)$  radially fixed at  $R_f = 3.9$  m. The final mirror of the 2-OLR antenna is steerable, so that the target position can be scanned toroidally and vertically, which changes the deposition location.

Then, the deposition location and the absorption power were evaluated using the ray-tracing code LHDGauss for various target positions and  $n_e$  profiles. Figures 1(b) and (c) show one example of ray-tracing calculations. Note that in Fig. 1(b) the data of zero absorption power are not depicted. Here, the deposition location,  $(r_{\text{eff}}/a_{99})_{\text{peak}}$ , is defined as the peak position of the radial profiles of the deposition power density, where  $r_{\text{eff}}/a_{99}$  means the effective minor radius normalized by the minor radius where 99% of the electron stored energy is confined. In the standard magnetic field configuration, there is no ECR layer near  $T_f = Z_f = 0$  m due to the magnetic field

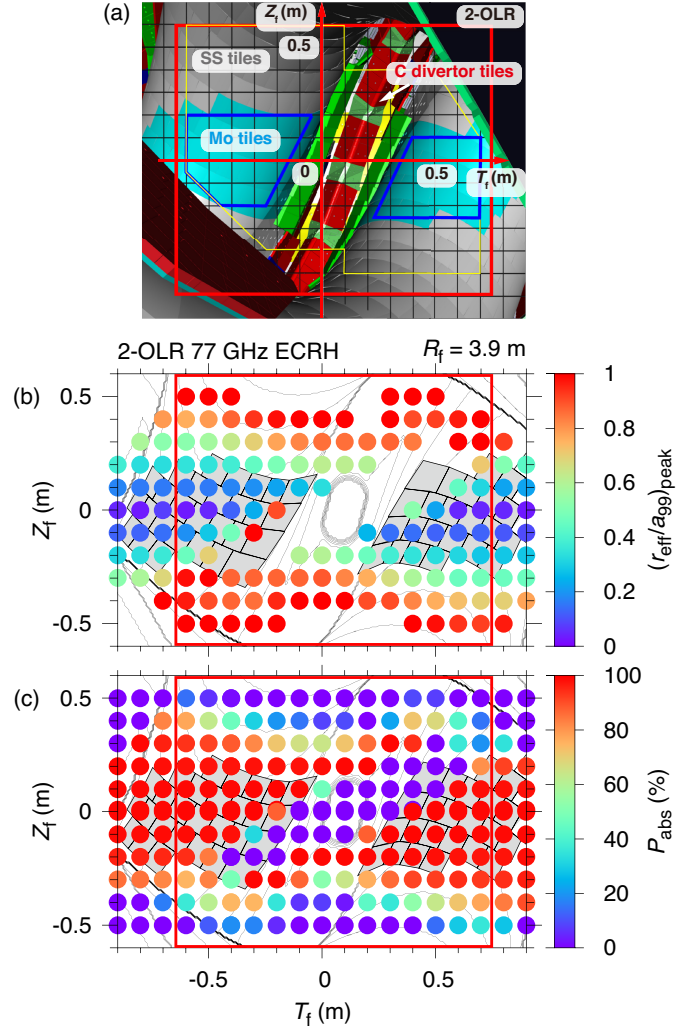


Figure 1: (a) A drawing viewed from the center of the final mirror of the 2-OLR antenna along with an imaginary target plane with a toroidally- and vertically-directed coordinate  $(T_f, Z_f)$  radially fixed at  $R_f = 3.9$  m, and a ray-tracing calculation example of (b) deposition locations and (c) power absorption efficiency for various target positions for  $n_{e,\text{avg}} \sim 1.0 \times 10^{19} \text{ m}^{-3}$  at  $t = 5$  s of the discharge #132433. The red square shows the steerable range of the mirror.

ripple, where no absorption is expected. Therefore, oblique injection is standard. One ECR layer passes near the magnetic axis in the case of oblique injection. In this case of the line-averaged density of  $n_{e,\text{avg}} \sim 1.0 \times 10^{19} \text{ m}^{-3}$ , on-axis heating with full absorption by the first pass can be realized by slightly oblique injection on the midplane.

Figure 2 illustrates the developed real-time deposition location control system. The data set on the relationship between deposition locations and target positions as well as  $n_e$  profiles were saved into FPGA memories in advance and referred to in real time. For the control using FPGA processing,  $n_e$  profiles are characterized with the following four parameters: electron density (i) at the magnetic axis,  $n_{e,\text{axis}}$ , (ii) at the last closed flux surface (LCFS),  $n_{e,\text{LCFS}}$ , and (iii) at the shoulder for hollow profiles,  $n_{e,\text{shoulder}}$ , and (iv) its shoulder position,  $(r_{\text{eff}}/a_{99})_{\text{shoulder}}$ . In the hollow  $n_e$  profile of

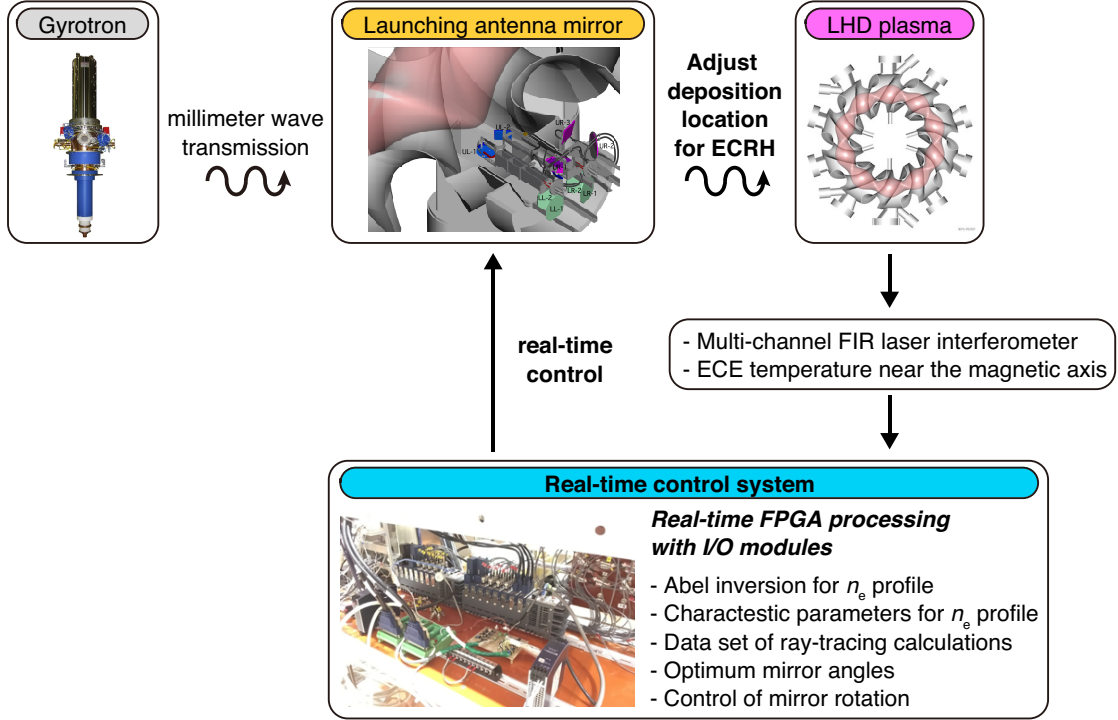


Figure 2: Schematic real-time control system of the deposition location of ECRH.

LHD plasmas, the peripheral region with a finite  $n_e$  gradient and strong magnetic shear is known to affect refraction and O-X mode coupling of the EC waves [1]. **For the real-time control of the EC wave polarization [12], only two parameters characterizing peripheral  $n_e$  profiles were used because O-X mode coupling of the EC wave occurs in the peripheral region.** The multi-channel far-infrared (FIR) laser interferometer [14] was adopted to obtain the  $n_e$  profile in real time, because the measurement is applicable to real-time diagnostics during long-pulse operations on the LHD. On the other hand, a real-time system similar to that developed at NSTX-U [15] is under consideration to be deployed at the multi-point Thomson scattering diagnostic of the LHD [16], which will provide  $n_e$  profiles in real time. The real-time acquisition of the  $n_e$  profile with the FIR laser interferometer was performed with real-time FPGA processing. The FPGA is included in a fast reliable hardware CompactRIO (cRIO) cRIO-9039 with its input/output modules made by National Instruments (NI) and communicated by its software through LabVIEW FPGA programming. **The cRIO-9039 controller embeds a reconfigurable Xilinx Kintex-7 325T FPGA with an on-board clock frequency of 40 MHz, 407600 flip-flops, 203800 look-up tables (LUT), 16020 kbits of block RAM, and 840 DSP (digital signal processor) slices.** Signals of line-integrated  $n_e$  measured with the FIR laser interferometer at major radii of  $R = 3.669, 3.759, 3.849, 3.939, 4.029, 4.119, \text{ and } 4.209$  m were inputted into cRIO. Transformation from the measured line-integrated  $n_e$  profile to the local  $n_e$  profile was performed by Abel inversion and implemented in FPGA. Fitting of the discrete  $n_e$  profile was also implemented in FPGA. For details of the processing regarding

$n_e$  profiles, refer to the previous work [12]. Then, the four parameters characterizing  $n_e$  profiles were calculated from the fitted profile and then discretized to be  $[0.5, 1, 2, 3, 4, 5] \times 10^{19} \text{ m}^{-3}$  for  $n_{e,\text{axis}}, n_{e,\text{LCFS}}, \text{ and } n_{e,\text{shoulder}}$ , and  $[0, 0.1, 0.2, \dots, 0.9]$  for  $(r_{\text{eff}}/a_{99})_{\text{shoulder}}$  in order to input the discretized parameters to the LUT of FPGA functions on cRIO under the limited capacity of FPGA.

The steering mirror of the 2-OLR antenna was rotated around two axes, i.e.,  $x$  and  $y$  axes, with a pair of low-inertia servo motors (Panasonic MSMD011G1A1) whose operational rotation speed was set 1600 rpm at maximum [17]. With the relationship between the motors and their encoders, each rotation speed around the two axes of the steering mirror was approximately  $2.1^\circ/\text{s}$  for  $x$  axis and  $2.7^\circ/\text{s}$  for  $y$  axis, respectively. Their rotation was controlled by a PLC (programmable logic controller) [17], **thus only** their rotation direction, i.e., clockwise or counterclockwise, was decided in FPGA through a digital output module NI 9477 installed on cRIO by comparing the command rotation angles and the real rotation angles. **The calculation cycle of the real-time deposition control was almost  $40 \mu\text{s}$  (1600 clocks).** Half of the logic resources of FPGA were used for the control when the four parameters characterizing  $n_e$  profiles were discretized as stated above.

In order to evaluate the performance of the steering mirror control, rotation of the two-axis mirror was controlled to follow square signals and sinusoidal signals, respectively, as shown in Figs. 3 and 4. Figure 3 shows time evolution of rotation angles of the two-axis steering mirror and resultant target positions during the rotation control. The execution time of

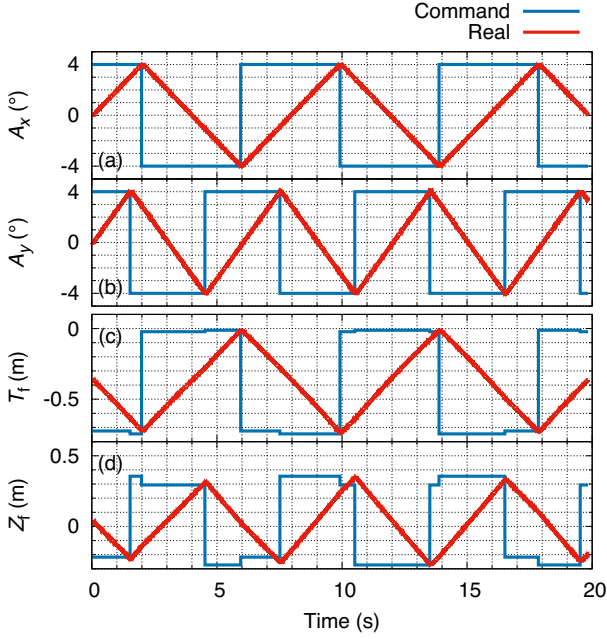


Figure 3: Time evolution of rotation angles of the steering mirror around (a)  $x$  axis and (b)  $y$  axis and resultant (c) toroidal and (d) vertical target positions during rotation control of the two-axis steering mirror under commands of square signals.

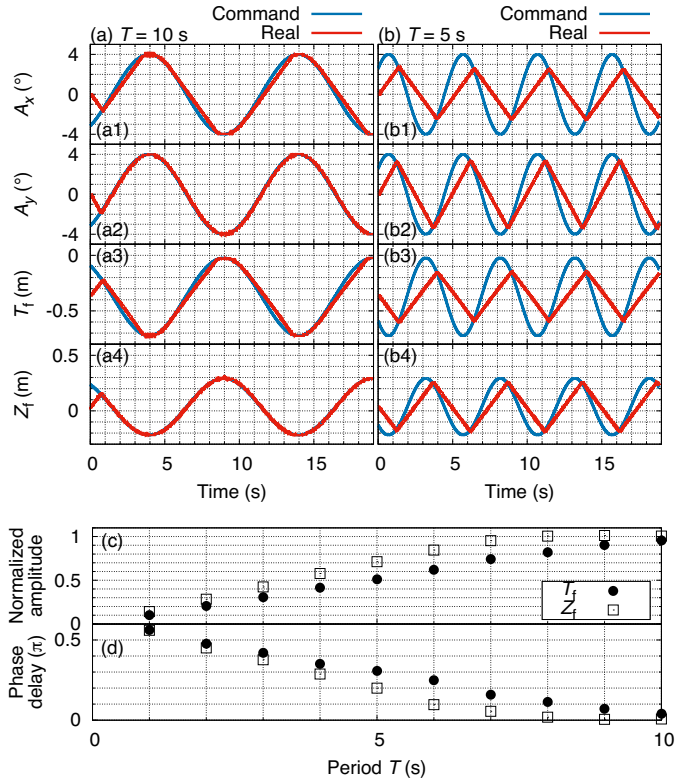


Figure 4: Time evolution of rotation angles of the two-axis steering mirror and resultant toroidal and vertical target positions at the period of (a) 10 s and (b) 5 s, respectively, and (c) the amplitude of real target positions normalized by the amplitude of the command signals and (d) phase delay from the command signals as a function of sinusoidal period.

one control loop was maintained for approximately 1 ms. The peak-to-peak amplitude of the square signal was set at  $8^\circ$ . The time periods were set properly to confirm that the rotation speeds were approximately  $2.1^\circ/\text{s}$  for  $x$  axis and  $2.7^\circ/\text{s}$  for  $y$  axis, which corresponded to 0.18 m/s in toroidal and 0.20 m/s in vertical on the imaginary target plane. The targeted area covers approximately 0.7 m toroidally and 0.5 m vertically, so that the radial deposition location can be scanned from the plasma core to the edge. Figures 4(a) and (b) show time evolution of rotation angles of the two-axis steering mirror and resultant target positions during the rotation control under commands of sinusoidal signals at the period of 10 s and 5 s, respectively. The steering mirror could follow the command rotation angles in the case of 10 s, although the control was delayed in the case of 5 s. Figures 4(c) and (d) show the amplitude of real target positions, oscillating at the frequency of the command signals, normalized by the amplitude of the command signals and the phase delay as a function of sinusoidal periods. It is confirmed that the toroidal target position can follow the command signal with a period of 10 s and the vertical target position can follow the command signal with a period larger than 8 s, while shorter periods cause a gradual increase in control delay and a gradual decrease in amplitude. This real-time control system can function properly in a long-pulse discharge for steady-state operation as long as command signals obtained by processing the FIR laser interferometer signals are generated.

### 3. Experiments of the real-time deposition location control on the LHD

In order to obtain and sustain high absorption power in ECRH under the EC wave refracted by time-varying  $n_e$ , real-time control of the deposition location of the 77-GHz EC wave launched from the 2-OLR antenna was demonstrated on the LHD. The injection power was 0.48 MW. ECRH plasmas were sustained by other gyrotrons. Figures 5 and 6 show a typical demonstrated result of the real-time deposition location control. The four parameters characterizing the  $n_e$  profile were calculated in real time using the signals measured with the FIR laser interferometer, as shown in Figs. 5(a)-(d). For comparison, those parameters calculated after the discharge from the  $n_e$  profile measured with the Thomson scattering diagnostics are also shown. These results show that there is not much difference between the four parameters processed from the line-integrated  $n_e$  profile with the FIR laser interferometer on the cRIO FPGA and those processed from the  $n_e$  profile with the Thomson scattering diagnostics, indicating that this real-time control system of the deposition location can provide the appropriate commands for the target positions. After discretization of the four parameters, the rotation angles of the steering mirror and the target positions were decided in real time from the beginning of the discharge through the data set of the ray-tracing calculations. Then, rotation control of the steering mirror was conducted from 3.5 s, as shown in Figs. 5(e) and (f). The command target positions were decided in order to obtain and sustain heating localized near the magnetic axis. The fluctuation seen in command signals, e.g. around 7 s,

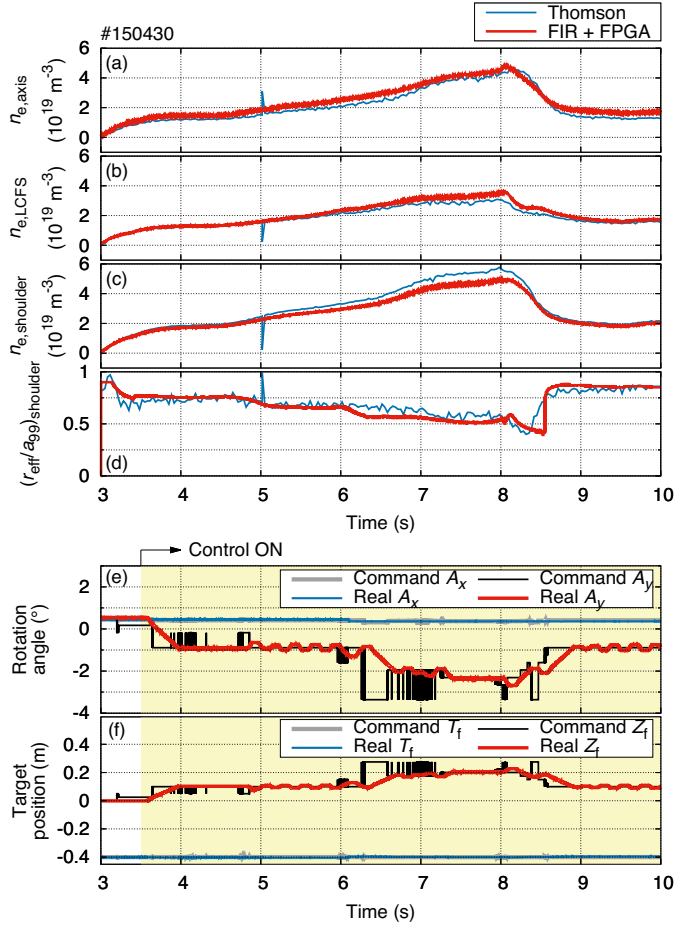


Figure 5: Time evolution of the four parameters regarding  $n_e$  profile: (a)  $n_{e,axis}$ , (b)  $n_{e,LCFS}$ , (c)  $n_{e,shoulder}$ , and (d)  $(r_{eff}/a_{99})_{shoulder}$ . (e) command and real rotation angles of the steering mirror, and (f) command and real target positions, respectively, during the real-time deposition location control. The four parameters regarding the  $n_e$  profile measured with the Thomson scattering diagnostics were also plotted on (a)-(d), respectively, for comparison. Rotation control of the steering mirror was conducted from 3.5 s.

was caused by discretization of the four parameters because the measured FIR laser interferometer signals were also fluctuating to affect discretization transiently. Since a deposition location can be controlled mainly by changing a vertical target position in general for an EC wave launched from an outer port at the LHD, the toroidal target position was fixed almost at  $T_f = -0.4$  m during the control, which is a normal operational setting of ECRH using the 2-OLR antenna. Since a high- $n_e$  plasma refracts the propagating EC beam vertically downward below the magnetic axis under this launch setting, the vertical target position must be set upward to compensate for the effect of refraction according to a gradual increase in  $n_e$ . The results shown in Figs. 5(e) and (f) indicate that rotation of the steering mirror was successfully controlled to follow the commands under the limited rotation speed, so that the requested target positions were accordingly realized.

Heating performance was compared between the cases with and without the control during  $n_e$  ramp-up discharges from  $1 \times 10^{19} \text{ m}^{-3}$  to  $4 \times 10^{19} \text{ m}^{-3}$ , as shown in Fig. 6. Note that the

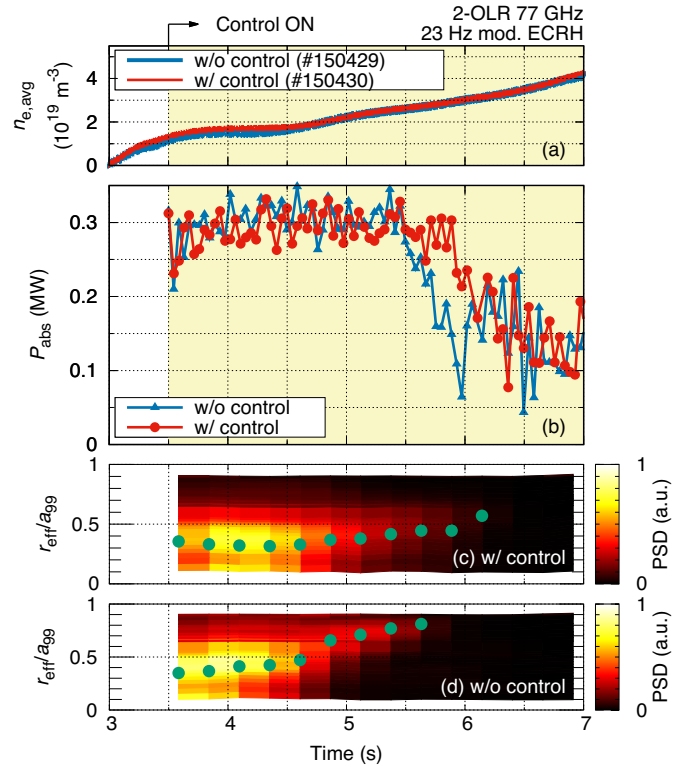


Figure 6: Time evolution of (a) line-averaged density, (b) absorption power, and radial profiles of the power spectral density (PSD) of  $T_e$  perturbation at the modulation ECRH frequency of 23 Hz in the cases (c) with and (d) without the real-time deposition location control. The deposition locations are also shown on the contours of each PSD in (c) and (d), respectively.

fundamental O-mode cutoff  $n_e$  is  $7.4 \times 10^{19} \text{ m}^{-3}$  for 77 GHz. The injection power from the 2-OLR antenna was modulated at the frequency of 23 Hz in order to evaluate the absorption power from change of the time derivative of the plasma stored energy at on/off timings [18]. In the case without the control from the beginning of the discharge, the steering mirror was fixed at the rotation angles the same as those in the case with the control before 3.5 s, i.e., before the start of the rotation control. When time  $t < 5$  s and  $n_{e,avg} \lesssim 2 \times 10^{19} \text{ m}^{-3}$ , the absorption power in the case with the control was as high as that in the case without the control. During that period, as shown in Figs. 6(c) and (d), which depict the radial profiles of the power spectral density (PSD) of  $T_e$  perturbation [19] by modulation ECRH at the frequency of 23 Hz, the peak location of the PSD, i.e., the deposition location, in the case with the control was maintained at  $(r_{eff}/a_{99})_{peak} \sim 0.3$ , while the deposition location in the case without the control shifted outward, which indicates that heating in the plasma core region was maintained longer due to the control. The deposition location calculated by the LHDGauss code is  $(r_{eff}/a_{99})_{peak} \sim 0.1$ , probably because the absorption of each ray is calculated with the quasi-perpendicular weakly relativistic model [10]. The neglected Doppler shift may affect broadening of the deposition profile in the case of oblique propagation of the EC wave. Then, after 5 s, the absorption power in the case without the control gradually decreases due to refraction of

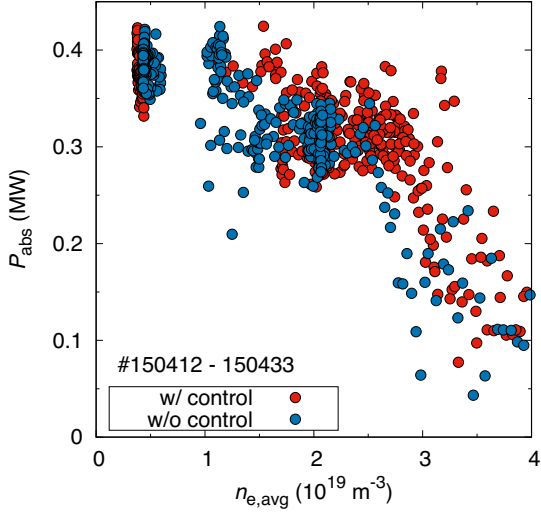


Figure 7: Dependence of the absorption power on the line-averaged density in the cases with and without the control.

the EC wave by gradual increase of  $n_{e,avg} \gtrsim 2 \times 10^{19} \text{ m}^{-3}$ , while higher absorption power was maintained longer due to the control under  $n_{e,avg} \lesssim 3 \times 10^{19} \text{ m}^{-3}$ . The decrease in the first-pass component of the absorption power in the case even with the control after  $n_{e,avg} \gtrsim 3 \times 10^{19} \text{ m}^{-3}$  was observed and the power level of absorption is almost the same as that in the case without the control, where refraction by the high- $n_e$  plasma deteriorates the first-pass absorption, suggesting that the effect of multi-pass absorption is expected to be dominant in the experimentally-evaluated absorption power.

Summarized results of the real-time deposition location control experiments are shown in Figs. 7 and 8, which show dependencies of the absorption power and the deposition location on  $n_{e,avg}$ . The results indicate that the control clearly improved the absorption power especially at  $1.5 \times 10^{19} \text{ m}^{-3} \lesssim n_{e,avg} \lesssim 3 \times 10^{19} \text{ m}^{-3}$  and that the control mitigated the deposition location shifting outward due to refraction of the EC wave at that  $n_{e,avg}$  range.

One of the causes for the effect of multi-pass absorption for  $n_{e,avg} \gtrsim 3 \times 10^{19} \text{ m}^{-3}$  is that purity of the first-pass O-mode EC wave decreases through propagation on the refracted orbit under the high- $n_e$  plasma. In that case, pure mode excitation is required on the refracted wave in order to increase the first-pass absorption. The new code “PARADE” is now under development [20, 21] for application to LHD plasmas. The code can calculate simultaneously refraction and O-X mode coupling of the EC beam propagating through the plasma periphery with finite magnetic shear, where the polarization of the EC wave can be affected, so that the calculation can contribute to optimizing the incident EC wave polarization under the refracted beam path for high- $n_e$  plasmas, which is a future work.

#### 4. Conclusion

The newly-developed real-time control system of the deposition location for ECRH in the LHD is described.

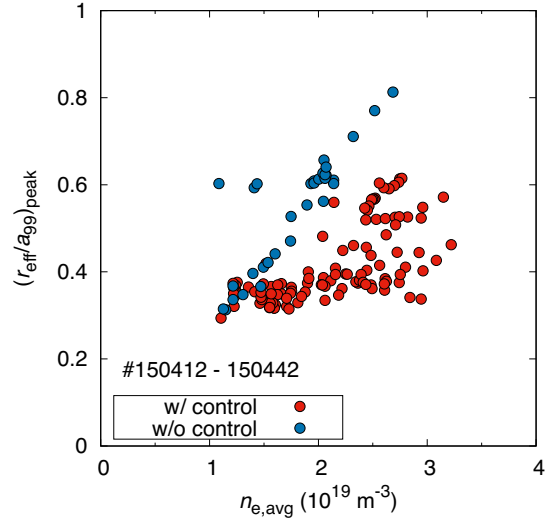


Figure 8: Dependence of the deposition location on the line-averaged density in the cases with and without the control.

Appropriate target positions were evaluated for various  $n_e$  profiles by calculating the deposition location and the absorption power by using the ray-tracing code LHDGauss. The calculated data set on the relationship between deposition locations and target positions as well as  $n_e$  profiles were saved into FPGA memories in advance and referred to in real time on the control system for adjusting the steering mirror of the launching antenna in order to improve the first-pass absorption of the refracted EC wave. The real-time deposition location control experiments on the LHD demonstrated that the absorption power was successfully maintained higher because the EC wave power was kept deposited in the plasma core region. In order to further improve the first-pass absorption, the incident polarization control on the refracted EC beam path along with the deposition location control can be helpful, which can result in purer heating mode excitation.

#### Acknowledgments

This work was supported in part by the National Institute for Fusion Science under grants ULRR027 and KLPH038, and by JSPS KAKENHI Grant Numbers 16K18338 and 19K14687.

#### References

- [1] T. I. Tsujimura *et al.*, Impact of the LHD peripheral region and the magnetic axis shift on optimal on-axis ECRH injection for high-electron-temperature plasmas, Preprint: 2016 IAEA Fusion Energy Conf. (Kyoto, Japan) IAEA-CN-234-0083 (<https://nucleus.iaea.org/sites/fusionportal/Shared%20Documents/FEC%202016/fec2016-preprints/preprint0083.pdf>).
- [2] E. Koleman *et al.*, Real-time mirror steering for improved closed loop neoclassical tearing mode suppression by electron cyclotron current drive in DIII-D, Fusion Eng. Des. 88 (2013) 2757.
- [3] M. Reich *et al.*, Real-time beam tracing for control of the deposition location of electron cyclotron waves, Fusion Eng. Des. 100 (2015) 73-80.
- [4] M. Joung *et al.*, Real Time MHD Mode Control Using ECCD in KSTAR: Plan and Requirements, AIP Conf. Proc. 1580 (2014) 506.

- [5] T. Kobayashi *et al.*, Density dependence of transient electron thermal transport property in LHD, *Nucl. Fusion* 58 (2018) 126031.
- [6] T. I. Tsujimura *et al.*, Optimization of Incident EC Wave Polarization in Real-Time Polarization Scan Experiments on LHD, *Plasma Fusion Res.* 11 (2016) 2402016.
- [7] H. Takahashi *et al.*, Extension of operational regime in high-temperature plasmas and effect of ECRH on ion thermal transport in the LHD, *Nucl. Fusion* 57 (2017) 086029.
- [8] F. Warmer *et al.*, Energy confinement of hydrogen and deuterium electron-root plasmas in the Large Helical Device, *Nucl. Fusion* 58 (2018) 106025.
- [9] K. Tanaka *et al.*, Isotope effects on energy, particle transport and turbulence in electron cyclotron resonant heating plasma of the Large Helical Device, *Nucl. Fusion* 59 (2019) 126040.
- [10] T. Ii Tsujimura *et al.*, Development and application of a ray-tracing code integrating with 3D equilibrium mapping in the LHD ECH experiments, *Nucl. Fusion* 55 (2015) 123019.
- [11] M. Emoto *et al.*, Automatically processing physical data from LHD experiments, *Fusion Eng. Des.* 89 (2014) 758.
- [12] T. Ii Tsujimura *et al.*, Real-time control of electron cyclotron wave polarization in the LHD, *Fusion Eng. Des.* 131 (2018) 130.
- [13] Y. Yoshimura *et al.*, Progress of long pulse discharges by ECH in LHD, *Nucl. Fusion* 56 (2016) 046005.
- [14] T. Akiyama *et al.*, Interferometer systems on LHD, *Fusion Sci. Technol.* 58 (2010) 352-363.
- [15] F. M. Laggner *et al.*, A scalable real-time framework for Thomson scattering analysis: Application to NSTX-U, *Rev. Sci. Instrum.* 90 (2019) 043501.
- [16] I. Yamada *et al.*, Calibrations of the LHD Thomson scattering system, *Rev. Sci. Instrum.* 87 (2016) 11E531.
- [17] K. Okada *et al.*, Development of fast steering mirror control system for plasma heating and diagnostics, *Rev. Sci. Instrum.* 85 (2014) 11E811.
- [18] R. Makino *et al.*, ECH absorbed power evaluation method compensated for temporal response of diamagnetic flux measurements on LHD, *JPS Conf. Proc.* 1 (2014) 015034, *Proc. 12th Asia Pacific Physics Conf.*
- [19] H. Tsuchiya *et al.*, Design and Installation of a New Electron Cyclotron Emission Diagnostic Antenna in LHD, *Plasma Fusion Res.* 6 (2011) 2402114.
- [20] K. Yanagihara *et al.*, Mode Purity of Electron Cyclotron Waves after Their Passage through the Peripheral Plasma in the Large Helical Device, *Plasma Fusion Res.* 14 (2019) 3403103.
- [21] I. Y. Dodin *et al.*, Quasioptical modeling of wave beams with and without mode conversion. I. Basic theory, *Phys. Plasmas* 26 (2019) 072110; K. Yanagihara *et al.*, Quasioptical modeling of wave beams with and without mode conversion. II. Numerical simulations of single-mode beams, *ibid.* 26 (2019) 072111; K. Yanagihara *et al.*, Quasioptical modeling of wave beams with and without mode conversion. III. Numerical simulations of mode-converting beams, *ibid.* 26 (2019) 072112.